HIGH BANDGAP ABSORBER FOR MONOLITHIC PEROVSKITE SILICON TANDEM SOLAR CELLS REACHING 25.1% CERTIFIED EFFICIENCY AND WAYS BEYOND

Patricia S. C. Schulze[1,2], Alexander J. Bett[1], Özde Ş. Kabaklı[1], Kristina M. Winkler[1], Laura E. Mundt[1,3], Fabian M. Gerspacher[1], Qinxin Zhang[1], Clarissa L. M. Hofmann[1,4], Martin Bivour[1], Martin Hermle[1], Stefan W. Glunz[1,5], Harald Hillebrecht[2], Jan Christoph Goldschmidt[1]

[1] Fraunhofer Institute for Solar Energy Systems, Heidenhofstr. 2, 79110 Freiburg, Germany
[2] Institute of Inorganic and Analytical Chemistry, University of Freiburg, 79104 Freiburg, Germany
[3] SLAC National Accelerator Laboratory, Stanford University, Stanford, CA, USA
[4] Institute of Microstructure Technology, Karlsruhe Institute of Technology, 76344 Eggenstein-Leopoldshafen, Germany
[5] Freiburg Center for Interactive Materials and Bioinspired Technologies (FIT) and Laboratory for Photovoltaic Energy Conversion, University of Freiburg, 79110 Freiburg, Germany

ABSTRACT: Perovskite silicon tandem solar cells (PSTSCs) can overcome the efficiency limitations of conventional single-junction silicon solar cells by reducing thermalization losses. To reach this goal, a perovskite absorber with an adapted high bandgap, good (photo-)stability, and high open-circuit voltage (V_{OC}) is needed. First approaches tried halide mixing with high bromide content but compounds suffered from light-induced halide segregation causing voltage losses. In this work, a balanced tuning approach for $[HC(NH_2)_2]_{1-x}Cs_xPb(I_{1-y}Br_y)_3$ perovskites is presented using reduced bromide content and compensating the bandgap effect by increasing the cesium(I) content. In that way, phase stability is reached while keeping the desired high bandgap. Moreover, surface passivation at the electron contact-perovskite interface highlights the important role of interfaces in the overall performance. $[HC(NH_2)_2]_{0.75}Cs_{0.25}Pb(I_{0.8}Br_{0.2})_3$ with an optical bandgap of ~1.69 eV is determined as the best candidate for tandem application. Implementation in monolithic PSTSCs with silicon heterojunction bottom solar cells enables high V_{OC} of ~1836 mV with excellent photostability in a mesoscopic n-i-p configuration, and high fill factor of 80% and 25.1% certified stabilized efficiency in a planar p-i-n configuration. Heading towards higher efficiencies, a hybrid co-evaporation/spin coating route is applied for easy bandgap tuning and conformal perovskite film formation on µm-sized random pyramid-textured silicon.
Keywords: Interfaces, Passivation, Perovskite, Silicon, Tandem

1 INTRODUCTION

Perovskite silicon tandem solar cells (PSTSCs) are promising candidates to overcome the theoretical limit of single-junction silicon solar cells that so far dominate the photovoltaic market. Taking Auger recombination into account, the maximum possible efficiency is 29.4% [1]. To exceed this limit, a second absorber material with a higher bandgap can be stacked on top in a tandem configuration to reduce thermalization losses. Calculations on complete PSTSC layer stacks predict a practical efficiency limit of 31 – 34% [2–4] with an optimum top cell bandgap in the range of 1.65 – 1.69 eV [2,3].

First PSTSCs were realized in 2015 with MAPbI$_3$ (MA for methylammonium $[CH_3NH_3]^+$) as perovskite absorber, which features a too low bandgap and limited stability, reaching 13.7% efficiency in a n-i-p configuration [5]. First attempts to increase the bandgap were based on halide mixing with high bromide content. However, such compounds suffer from light-induced halide segregation [6], and reduced open-circuit voltage (V_{OC}) in solar cells [7]. In 2016, McMeekin et al. [8] proposed $FA_{0.83}Cs_{0.17}Pb(I_{0.6}Br_{0.4})_3$ (FA for formamidinium $[HC(NH_2)_2]^+$) with a bandgap of 1.74 eV as promising candidate for the Si-based tandem application. Improved phase stability was reported due to incorporation of cesium(I) in such mixed cation lead mixed halide perovskites. Bush and Palmstrom et al. [9] introduced a related absorber, $FA_{0.83}Cs_{0.17}Pb(I_{0.83}Br_{0.17})_3$ with an optical bandgap of 1.63 eV, achieving 23.6% efficiency in the first PSTSCs with inverted p-i-n configuration with thin charge transport layers. Sahli and Werner et al. then demonstrated the first double-side textured perovskite silicon tandem device with a related absorber deposited by a hybrid evaporation/spin coating route reaching 25.2%

efficiency [10]. Since then, several groups reported on p-i-n perovskite silicon tandem devices surpassing 25% efficiency implementing mixed cation lead mixed halide perovskites [3,11–16]. The latest records by Oxford PV [17] and Helmholtz Zentrum Berlin [18] even reached 28.0% and 29.15% certified efficiency, respectively. However, no details on these record devices are available.

In this work, we present our development of high bandgap perovskite absorbers for application in monolithic PSTSCs. First, balanced bandgap tuning of the $x{:}y$ ratio is presented for $FA_{1-x}Cs_xPb(I_{1-y}Br_y)_3$ perovskite absorbers to achieve photostability and high voltage for an optimum bandgap of ~1.69 eV. To reach high voltage, surface passivation is implemented at the electron contact-perovskite interface. Furthermore, the best candidate $FA_{0.75}Cs_{0.25}Pb(I_{0.8}Br_{0.2})_3$ is tested in monolithic PSTSCs both in the classical mesoporous (mp) TiO$_2$-based n-i-p configuration and the inverted planar p-i-n configuration. Whereas n-i-p tandems allow for excellent V_{OC} but limited current, the p-i-n tandems allow for high fill factor (*FF*) and highest efficiency of 25.1%. Heading towards higher efficiencies in double-side textured tandems, the perovskite deposition is transferred to a hybrid co-evaporation/spin coating route enabling easy bandgap tuning and conformal perovskite film formation on µm-sized random pyramid-textured silicon.

2 EXPERIMENTALS

2.1 Device fabrication

Silicon heterojunction bottom solar cells were fabricated from 200 µm (n-type) and 250 µm (p-type) thick silicon float zone wafers with a resistivity of 1 Ω cm. Fabrication details can be found in [16,19]. Wafers were

cut in 2.5 cm × 2.5 cm substrates.

Perovskite top solar cells in the mesoporous n-i-p configuration consist of ITO/compact (c-)TiO$_2$/mp-TiO$_2$/ perovskite/doped 2,2',7,7'-tetrakis-[*N,N*-di(4-methoxy-phenyl)amino]-9,9'-spirobifluorene (Spiro-OMeTAD)/ ITO/Au busbar/MgF$_2$. An adapted ITO process allows for direct sputtering on Spiro-OMeTAD without any buffer layer protection [20]. The TiO$_2$ electron contact was fabricated via a developed low-temperature process route (≤ 120°C) [21]. A blend of [6,6]-phenyl-C$_{61}$-butyric acid methyl ester and polymethyl methacrylate (PCBM-PMMA) was applied for surface passivation on mp-TiO$_2$ based on Peng et al. [22].

In the p-i-n configuration, top solar cells consist of poly[bis(4-phenyl)(2,4,6-trimethyl-phenyl)-amine] (PTAA)/ poly(9,9-bis(3'-(*N,N*-dimethyl)-*N*-ethyl-ammo-nium-propyl-2,7-fluorene)-alt-2,7-(9,9-dioctylfluorene))-dibromide (PFN-Br)/perovskite/C$_{60}$/SnO$_x$/ITO/Ag busbar/MgF$_2$. The interconnection and front contact ITO was deposited through a shadow mask defining four individual tandem solar cells (6 mm×6 mm openings) on each substrate. Further information is described in our previous publications on PSTSCs [16,19].

Perovskite single-junction solar cells were fabricated on ITO-coated glass and finished with a full-area metal contact. No front ITO and ARC depositions were applied.

Concerning the perovskite absorber, balanced tuning of FA$_{1-x}$Cs$_x$Pb(I$_{1-y}$Br$_y$)$_3$ compositions was carried out via stoichiometric weighing of formamidinium iodide (FAI), cesium(I) iodide (CsI), lead(II) bromide (PbBr$_2$), and lead(II) iodide (PbI$_2$). The common one-step spin coating route using the anti-solvent method (toluene) was applied for perovskite deposition, followed by annealing. The precursor molarity of 1.0 M used in n-i-p devices was optimized to 1.1 M and applied in p-i-n devices.

In case of the two-step hybrid co-evaporation/spin coating route, PbI$_2$ and CsI were thermally co-evaporated in a first step. A mass ratio of 17/100 for Cs/Pb was manually controlled via the deposition rates. In the second step, mixtures of FABr/FAI were spin coated on top of the inorganic scaffold, followed by annealing.

Further details can be found in previously published publications [16,19,23].

2.2 Characterization

Optical analysis was carried out using a Lambda 950 spectrophotometer from PerkinElmer equipped with an integrating sphere. Grazing incidence X-ray diffraction (GIXRD) was performed with a X'Pert MRD system (PANalytical) equipped with a copper anode X-ray source ($\lambda_{K\alpha1}$ = 1.5406 Å). Current-voltage (*I-V*) characteristics of single-junction solar cells were carried out at a sun simulator equipped with a xenon short arc lamp and a source meter with a scan speed of 43 mV/s. Tandem solar cells with n-i-p configuration were measured using a LED sun simulator (Wavelabs, Sinus-220) with a scan speed of 25 mV/s. For both simulators, the light intensity was calibrated to the AM1.5g spectrum using a silicon reference cell. A mask defines an active cell area of 0.25 cm^2. For certified results, p-i-n solar cells were measured at Fraunhofer ISE CalLab PV Cells considering spectral mismatch. Photoluminescence (PL) mapping and time series under constant illumination were conducted using a confocal microscope with a cold light beam splitter. The perovskite layer was probed with a frequency-doubled Nd:YAG solid state laser (532 nm, 0.5 µW/µm^2). Scanning electron microscopy (SEM) images were taken

at a Schottky emission SEM (Zeiss, Auriga 60) at 5 kV. More detailed information can be found in previous publications [16,19,23,24].

3 RESULTS

3.1 High bandgap absorber

Compositional engineering of FA$_{1-x}$Cs$_x$Pb(I$_{1-y}$Br$_y$)$_3$ mixed cation lead mixed halide perovskites was carried out using a balanced tuning approach. Based on the work of McMeekin et al. [8] and Bush et al. [25], *x* and *y* were altered simultaneously (reducing bromide, while increasing cesium(I)) to keep the desired bandgap of ~1.69 eV and identify compositions with improved photovoltaic performance and photostability. Figure 1 shows results from optical and structural analysis of tested compositions.
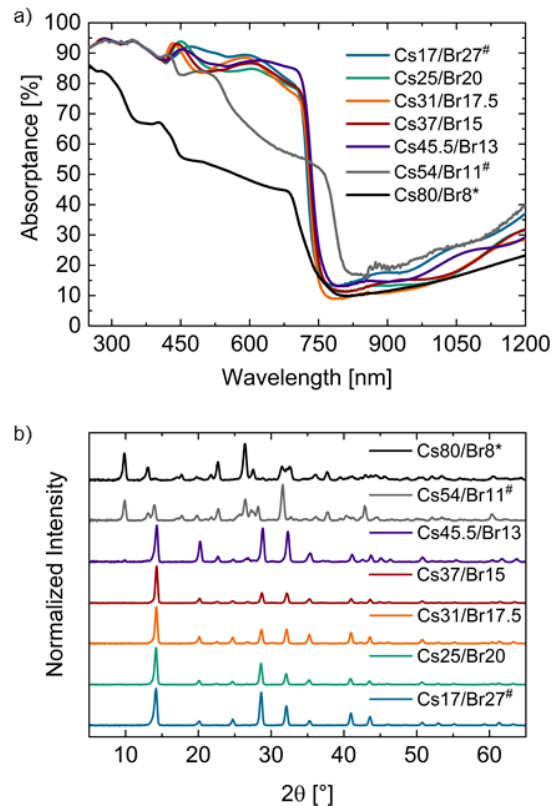

Figure 1: (a) Optical and (b) structural analysis of FA$_{1-x}$Cs$_x$Pb(I$_{1-y}$Br$_y$)$_3$ perovskites studied with compositional engineering [19]. Abbreviations are assigned to each composition, e.g. Cs17/Br27 for FA$_{0.83}$Cs$_{0.17}$Pb(I$_{0.73}$Br$_{0.27}$)$_3$. Samples labelled with * and # are deposited without a Spiro-OMeTAD capping layer and on fluorine-doped tin oxide-coated substrates, respectively. For increasing Cs content, the (100) main perovskite reflection shifts to higher 2θ-values. For Cs contents above 45.5% no perovskite phase is formed anymore.

An impact of the compositional change on crystallization and film formation can already be observed during processing; dark films are formed except for high Cs contents (Cs54/Br11, Cs80/Br8), which yield turbid, light brown films. High absorptance and a desired optical bandgap of 1.69 eV are present for films with Cs contents up to 45.5%. Thin film diffraction analysis reveals that the cubic perovskite structure is not formed anymore for

higher Cs contents, which is in good accordance with literature [26]. A closer look at the reflection in the (100) plane shows a shift towards higher 2θ values for increasing Cs amount - correlating to a reduction of the lattice parameter and unit cell volume - before the perovskite structure breaks down. Compositions with high Cs contents, like Cs54/Br11 and Cs80/Br8, can therefore be excluded from application in solar cells. For Cs54/Br11, the diffraction pattern shows good agreement with the ternary orthorhombic $CsPbI_3$ phase (ICSD 161480). It is noted that from Cs25/Br20 on, small traces of this phase are already present (visible at 22.7°) and increase with rising Cs content.

Implementation of the absorbers in low-temperature processed n-i-p single-junction solar cells revealed an influence of the compositional changes on the photovoltaic performance (Figure 2). Best V_{OC} and efficiency was obtained for Cs25/Br20 with a PMMA-PCBM passivation layer at the TiO_2-perovskite interface. The surface passivation yielded a significant increase in V_{OC} of high bandgap perovskite solar cells. Compositions with higher Cs contents (Cs37/15, Cs45.5/Br13) revealed reduced V_{OC} and pronounced hysteresis with low *FF* in forward scan direction (not shown).
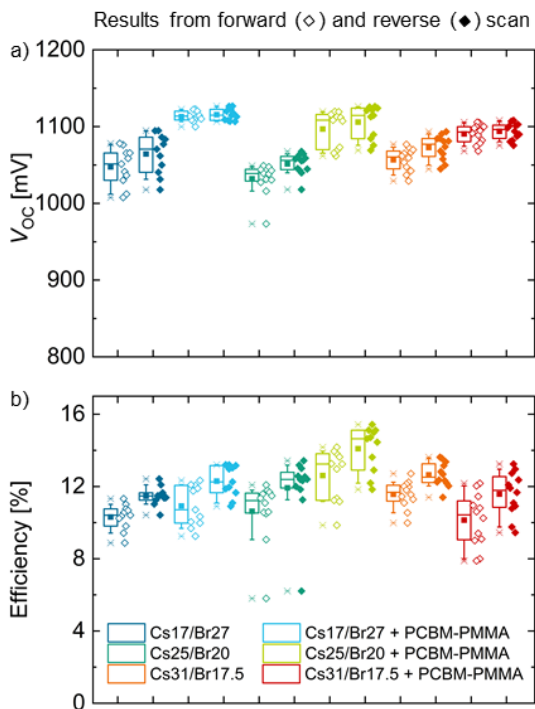

Figure 2: Box plots of (a) the V_{OC} and (b) the efficiency of high bandgap perovskite solar cells without/with a PCBM-PMMA passivation layer between the electron contact-perovskite interface [19]. Boxplots include 50% of the data points within the boxes and 80% within the whiskers. A horizontal line and point in the boxes represent the median and mean value, respectively. A significant V_{OC} improvement is present for passivated solar cells, especially for the Cs25/Br20 perovskite composition.

3.2 Tandem devices

Silicon heterojunction bottom solar cells (one sun iV_{OC} >700 mV) were combined with a mesoscopic and a planar perovskite top solar cell in the n-i-p and p-i-n device configuration, respectively (see Figure 3).
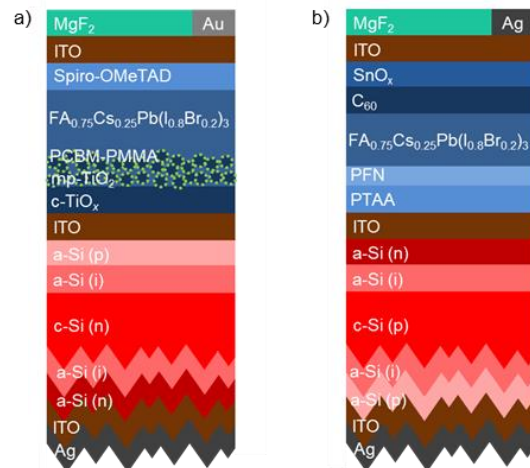

Figure 3: Investigated device architectures of monolithic PSTSCs using the high bandgap absorber (a) in a mesoscopic n-i-p configuration and (b) in a planar p-i-n configuration.

Figure 4 presents a sub-cell selective and spatially resolved PL characterization of the optimized perovskite absorber Cs25/Br20 implemented in a n-i-p tandem device (device architecture see Figure 3a). The perovskite absorber shows a homogeneous bandgap over the substrate and is photostable over time under continuous illumination. In contrast photoinstable perovskite compositions show a characteristic red shift [6] to ~1.65 eV within a few seconds under constant illumination, which is not the case here.
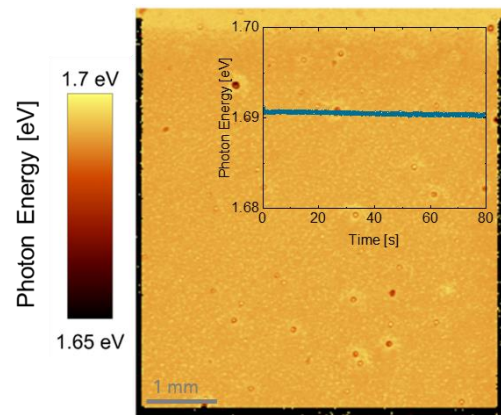

Figure 4: Representative sub-cell selective and spatially resolved PL mapping of the perovskite top cell in a n-i-p tandem solar cell with the optimized perovskite absorber Cs25/Br20 [19]. The inset shows the PL peak position of a spot over time. The perovskite absorber features a photostable PL peak position at 1.69 eV and excellent spatial homogeneity over the solar cell area.

Table I presents the best photovoltaic parameters of the optimized high bandgap perovskite absorber in monolithic PSTSCs using the mesoscopic n-i-p and the planar p-i-n device architecture, respectively. In the n-i-p configuration, a high V_{OC} of ~1836 mV is achieved, which corresponds to almost loss-free addition of the V_{OC}s of the sub-cells. A stabilized efficiency of 21.6% is determined from a fixed voltage measurement over 30 min (@V_{MPP} determined from *I-V* scans). The tandem performance is clearly limited by the low current of ~15.3 mA/cm².

Optical and spectrometric analysis revealed that the perovskite top cell is current-limiting, which mainly arises from an optically unsuitable front contact stack and parasitic absorption in the thick Spiro-OMeTAD layer. Implementation of the high bandgap absorber in the inverted p-i-n device polarity, using thin charge transport material and a 10% increased precursor molarity, enabled a significant improvement of the J_{SC} of 2.4 mA/cm^2. Also the *FF* was improved. The V_{OC}, however, decreased by 64 mV. A certified stabilized efficiency of 25.1% is achieved. The voltage loss in p-i-n tandem devices was attributed to surface recombination and leaves room for improvement by implementation of passivation layers, especially at the perovskite-C$_{60}$ interface [16]. Assuming the same high V_{OC} in p-i-n devices as obtained in n-i-p devices, efficiency increases to 26%. Mitigation of remaining reflection losses (5.5 mA/cm^2), e.g. with more advanced anti-reflection foils, and realization of a matched current of 20 mA/cm^2 as already presented in literature [27] would enable 29.4% efficiency. Consequently, the full potential of the high bandgap absorber has not been unlocked, yet.

Table I: Photovoltaic parameters of monolithic PSTSCs implementing the high bandgap absorber in the mesoscopic n-i-p [19] and the planar p-i-n [16] device architecture. The p-i-n device was measured at Fraunhofer ISE CalLab PV Cells (*certified). Highest efficiency is reached for the p-i-n device architecture.

		J_{SC} [mA/cm^2]	V_{OC} [mV]	*FF* [%]	Eff. [%]	Stab. eff. [%]
n-i-p Tandem	for	15.3	1834	75	21.1	21.6
	rev	15.2	1837	77	21.6	
*p-i-n Tandem	for	17.6	1774	75	23.3	25.1
	rev	17.7	1770	80	25.1	

3.2 Deposition on texture

To reach highest efficiency, light management plays an important role. In this respect, fully textured tandem solar cells with μm-sized random pyramid texture at the front and rear side are of particular interest. However, conformal layer formation with the common wet chemical spin coating method remains challenging on large textures. Instead, we investigate a hybrid co-evaporation/spin coating deposition method for promising FA$_{1-x}$Cs$_x$Pb(I$_{1-y}$Br$_y$)$_3$ compositions [23]. In a first step, the inorganic scaffold consisting of PbI$_2$ and CsI is co-evaporated. In a second step, the organic components FABr and FAI are dissolved in iso-propanol and spin-coated on the scaffold. By control of the FABr:FAI ratio systematic bandgap tuning from 1.54 - 1.75 eV is possible [23]. Subsequent annealing gives a conformal perovskite thin film with desired bandgap on μm-sized random pyramid-textured silicon. Figure 5 shows a cross-sectional SEM image after the deposition of the inorganic scaffold (1st step) and after deposition of the organic components and annealing (2nd step) for a high bandgap perovskite with an adapted optical bandgap of 1.7 eV. A conformal layer deposition is achieved thanks to the conformal scaffold formation in the 1st step. Its plate-like morphology allows for infiltration of the organic solution and full conversion to perovskite in the 2nd step. Thus, the hybrid deposition route allows for implementation of the high bandgap perovskite absorber also in fully textured perovskite silicon tandem devices.
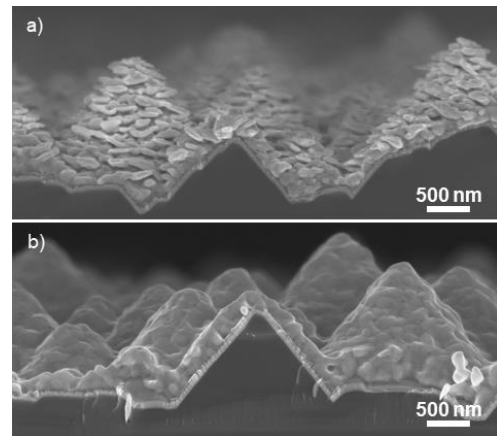

Figure 5: SEM cross-sectional images of the hybrid co-evaporation/spin coating for FA$_{1-x}$Cs$_x$Pb(I$_{1-y}$Br$_y$)$_3$ perovskites [23]. (a) After the 1st step co-evaporation of the inorganic scaffold, and (b) after the 2nd step spin coating of the organic components and annealing. Conformal high bandgap perovskite thin films (here shown for 1.7 eV) cover μm-sized random pyramid-textured silicon.

4 CONCLUSION

FA$_{1-x}$Cs$_x$Pb(I$_{1-y}$Br$_y$)$_3$ high bandgap perovskite absorbers featuring an optimum optical bandgap of ~1.69 eV were investigated. The balanced tuning approach revealed that increasing the Cs amount counterbalances a reduction of Br to a certain extent, enabling to mitigate phase instability under illumination and keep the optimum high bandgap. FA$_{0.75}$Cs$_{0.25}$Pb(I$_{0.8}$Br$_{0.2}$)$_3$ has proven to be the best candidate for tandem application. Applied passivation at the electron contact-perovskite interface additionally helped improving V_{OC} and efficiency without reducing the *FF*. This highlights the important role of interfaces in the overall performance of high bandgap solar cells.

Implementation of the high bandgap absorber in both, mesoporous n-i-p and planar p-i-n monolithic PSTSCs reached 21.6% and 25.1% (certified) efficiency, respectively. Excellent V_{OC} of ~1836 mV but low J_{SC} are present in the n-i-p configuration. Here, the front contact is limiting the performance. In the p-i-n configuration improved J_{SC} but reduced V_{OC} are present. In this case, surface recombination is limiting the performance. Based on our analysis we conclude that with surface passivation along with improved anti-reflection measures the high bandgap perovskite absorber has the potential for 29% tandem efficiency in the near future (one-side rear texture).

Heading towards fully textured perovskite silicon tandem devices, the wet chemical spin coating route of the perovskite absorber was replaced by a hybrid co-evaporation/spin coating route, enabling easy bandgap adaptation to 1.70 eV and a conformal perovskite layer formation on μm-sized random pyramid-textured silicon

5 REFERENCES

[1] A. Richter, M. Hermle, S.W. Glunz, IEEE Journal of Photovoltaics 3 (2013) 1184–1191.

[2] M.T. Hörantner, H.J. Snaith, Energy & Environmental Science 10 (2017) 1983–1993.

[3] M. Jošt, E. Köhnen, A. Morales Vilches, B. Lipovšek, K. Jäger, B. Macco, A. Al-Ashouri, J. Krc, L. Korte, B. Rech, R. Schlatmann, M. Topic, B. Stannowski, S. Albrecht, Energy & Environmental Science 11 (2019) 3511–3523.

[4] K. Jäger, L. Korte, B. Rech, S. Albrecht, Optics Express 25 (2017) A473–A482.

[5] J.P. Mailoa, C.D. Bailie, E.C. Johlin, E.T. Hoke, A.J. Akey, W.H. Nguyen, M.D. McGehee, T. Buonassisi, Applied Physics Letters 106 (2015) 121105.

[6] E.T. Hoke, D.J. Slotcavage, E.R. Dohner, A.R. Bowring, H.I. Karunadasa, M.D. McGehee, Chemical Science 6 (2015) 613–617.

[7] E.L. Unger, L. Kegelmann, K. Suchan, D. Sörell, L. Korte, S. Albrecht, Journal of Materials Chemistry A 5 (2017) 11401–11409.

[8] D.P. McMeekin, G. Sadoughi, W. Rehman, G.E. Eperon, M. Saliba, M.T. Horantner, A. Haghighirad, N. Sakai, L. Korte, B. Rech, M.B. Johnston, L.M. Herz, H.J. Snaith, Science 351 (2016) 151–155.

[9] K.A. Bush, A.F. Palmstrom, Z.J. Yu, M. Boccard, R. Cheacharoen, J.P. Mailoa, D.P. McMeekin, R.L.Z. Hoye, C.D. Bailie, T. Leijtens, I.M. Peters, M.C. Minichetti, N. Rolston, R. Prasanna, S. Sofia, D. Harwood, W. Ma, F. Moghadam, H.J. Snaith, T. Buonassisi, Z.C. Holman, S.F. Bent, M.D. McGehee, Nature Energy 2 (2017) 17009.

[10] F. Sahli, J. Werner, B.A. Kamino, M. Bräuninger, R. Monnard, B. Paviet-Salomon, L. Barraud, L. Ding, J.J. Diaz Leon, D. Sacchetto, G. Cattaneo, M. Despeisse, M. Boccard, S. Nicolay, Q. Jeangros, B. Niesen, C. Ballif, Nature materials 17 (2018) 820–826.

[11] E. Köhnen, M. Jošt, A. Morales Vilches, P. Tockhorn, A. Al-Ashouri, B. Macco, L. Kegelmann, L. Korte, B. Rech, R. Schlatmann, B. Stannowski, S. Albrecht, Sustainable Energy Fuels 3 (2019) 1995–2005.

[12] K.A. Bush, S. Manzoor, K. Frohna, Z.J. Yu, J.A. Raiford, A.F. Palmstrom, H.-P. Wang, R. Prasanna, S.F. Bent, Z.C. Holman, M.D. McGehee, ACS Energy Letters 3 (2018) 2173–2180.

[13] B. Chen, Z. Yu, K. Liu, X. Zheng, Y. Liu, J. Shi, D. Spronk, P.N. Rudd, Z. Holman, J. Huang, Joule 3 (2019) 177–190.

[14] L. Mazzarella, Y.-H. Lin, S. Kirner, A.B. Morales-Vilches, L. Korte, S. Albrecht, E. Crossland, B. Stannowski, C. Case, H.J. Snaith, R. Schlatmann, Advanced Energy Materials 9 (2019) 1803241.

[15] J. Xu, C.C. Boyd, Z.J. Yu, A.F. Palmstrom, D.J. Witter, B.W. Larson, R.M. France, J. Werner, S.P. Harvey, E.J. Wolf, W. Weigand, S. Manzoor, van Hest, Maikel F. A. M., J.J. Berry, J.M. Luther, Z.C. Holman, M.D. McGehee, Science 367 (2020) 1097–1104.

[16] P.S.C. Schulze, A.J. Bett, M. Bivour, P. Caprioglio, F.M. Gerspacher, Ö.Ş. Kabaklı, A. Richter, M. Stolterfoht, Q. Zhang, D. Neher, M. Hermle, H. Hillebrecht, S.W. Glunz, J.C. Goldschmidt, Sol. RRL 4 (2020) 2000152.

[17] Oxford PV, Oxford PV perovskite solar cell achieves 28% efficiency, 2018, https://www.oxfordpv.com/news/oxford-pv-perovskite-solar-cell-achieves-28-efficiency, accessed 13 November 2019.

[18] Helmholtz Zentrum Berlin, World Record: Efficiency of perovskite silicon tandem solar cell jumps to 29.15 per cent, 2020, https://www.helmholtz-berlin.de/pubbin/news_seite?nid=21020;sprache=en;seitenid=, accessed 24 February 2020.

[19] A.J. Bett, P.S.C. Schulze, K.M. Winkler, Ö.S. Kabakli, I. Ketterer, L.E. Mundt, S.K. Reichmuth, G. Siefer, L. Cojocaru, L. Tutsch, M. Bivour, M. Hermle, S.W. Glunz, J.C. Goldschmidt, Progress in Photovoltaics: Research and Applications 28 (2019) 99–110.

[20] A.J. Bett, K.M. Winkler, M. Bivour, L. Cojocaru, Ö.S. Kabakli, P.S.C. Schulze, G. Siefer, L. Tutsch, M. Hermle, S.W. Glunz, J.C. Goldschmidt, ACS applied materials & interfaces 11 (2019) 45796–45804.

[21] P.S.C. Schulze, A.J. Bett, K. Winkler, A. Hinsch, S. Lee, S. Mastroianni, L.E. Mundt, M. Mundus, U. Würfel, S.W. Glunz, M. Hermle, J.C. Goldschmidt, ACS applied materials & interfaces 9 (2017) 30567–30574.

[22] J. Peng, Y. Wu, W. Ye, D.A. Jacobs, H. Shen, X. Fu, Y. Wan, T. Duong, N. Wu, C. Barugkin, H.T. Nguyen, D. Zhong, J. Li, T. Lu, Y. Liu, M.N. Lockrey, K.J. Weber, K.R. Catchpole, T.P. White, Energy & Environmental Science 10 (2017) 1792–1800.

[23] P.S.C. Schulze, K. Wienands, A.J. Bett, S. Rafizadeh, L.E. Mundt, L. Cojocaru, M. Hermle, S.W. Glunz, H. Hillebrecht, J.C. Goldschmidt, Thin Solid Films 704 (2020) 137970.

[24] L.E. Mundt, F.D. Heinz, S. Albrecht, M. Mundus, M. Saliba, J.P. Correa-Baena, E.H. Anaraki, L. Korte, M. Gratzel, A. Hagfeldt, B. Rech, M.C. Schubert, S.W. Glunz, IEEE Journal of Photovoltaics 7 (2017) 1081–1086.

[25] K.A. Bush, K. Frohna, R. Prasanna, R.E. Beal, T. Leijtens, S.A. Swifter, M.D. McGehee, ACS Energy Letters 3 (2018) 428–435.

[26] R. Prasanna, A. Gold-Parker, T. Leijtens, B. Conings, A. Babayigit, H.-G. Boyen, M.F. Toney, M.D. McGehee, Journal of the American Chemical Society 139 (2017) 11117–11124.

[27] M.A. Green, Y. Hishikawa, E.D. Dunlop, D.H. Levi, J. Hohl-Ebinger, M. Yoshita, A.W.Y. Ho-Baillie, Progress in Photovoltaics: Research and Applications 27 (2019) 3–12.